Experimental and numerical study on the bending behavior of glass-fabric rubber composites

Oguz Kagan Genc, Fabrice Schmidt, Steven Marguet, Gilles Dusserre, Pablo Navarro, Alice Courtois, Amina H. Brahami, Nathan Selles

EXPERIMENTAL AND NUMERICAL STUDY ON THE BENDING BEHAVIOR OF GLASS-FABRIC RUBBER COMPOSITES

Oguz Kagan GENC[1,2*], Fabrice Schmidt[1], Steven Marguet[1], Gilles Dusserre[1], Pablo Navarro[1], Alice Courtois[2], Amina H. Brahami[3], Nathan Selles[3]

[1]Institut Clément Ader (ICA), Université de Toulouse, CNRS, IMT Mines Albi, INSA, ISAE SUPAERO, UT, 3 Rue Caroline Aigle d'Aigle, 31400 Toulouse, France
Web page : https://ica.cnrs.fr

[2]Airbus Operations SAS, 316 route de Bayonne, 31060 Toulouse, France
Web page : https://www.airbus.com/en

[3]Elanova Laboratory, 60 rue Auber, 94408 Vitry-sur-Seine, France
Web page : https://elanova.fr/

Keywords: Elastomer matrix composites, Fabrics, Anisotropic hyperelasticity, Identification, Properties, Computational modelling, Finite element modelling

ABSTRACT

The study mainly focuses on the instantaneous mechanical behavior of glass-fabric rubber composites. Aside from principal-invariant-driven isotropic hyperelasticity, the strain energy contribution of fabric layer to the overall constitutive behavior of the composite can be defined by pseudo-invariant-driven anisotropic hyperelasticity. The approach accounts for the anisotropy of the silicone rubber matrix reinforced by plain-wave glass fabric using pseudo-invariants defined by vectors aligned with the warp and weft directions. Subsequently, the composite specimens with 0- and 45-degree fabric orientations were considered for the uniaxial tensile tests on top of the tests on pure rubber under different modes. The parameters of the analytical models with the above-mentioned approach were then identified from the test results. Moreover, different anisotropic hyperelastic material models were scripted and subsequently implemented into Abaqus using the UANISOHYPER_INV material subroutine. After checking the developed material subroutines with the coupon tests, this paper constructively paves a path to delve deeper into bending behavior of fabric rubber composites with the developed methodology accompanied with 3-point bending tests.

1 INTRODUCTION

Fabric rubber composites have been prominently utilized in industries such as space [1], aerospace [2-4], and automotive [5] due to their great sealing capacity and durability under harsh environmental conditions. In particular to aero-engine seals, the sealing performance is directly correlated to engine performance since they reduce leakage and optimize clearances [6,7]. Sealing of the cooling systems in aero-engines also greatly contributes to the performance by controlling clearances, as seen in Fig. 1 from the Turbine Case Cooling (TCC) seal improvement on High-Pressure Turbine (HPT) tip clearance [7]. An example of TCC seal is also provided in Fig. 2 [8].

On top of the performance contributions of seals, aero-structure seal malfunctioning would result in serious consequences, as highlighted by Shabbir [9]. In the same study, it was noted that a design defect in the knife edge seal of Pratt&Whitney's (P&W) GTF (geared turbofan engine) on Airbus A320neo caused sudden shutdowns during flight or take-off, resulting in a call back of these engines. Similarly, the failure of the Auxiliary Power Unit compressor carbon seal caused oil leakage and subsequent heavy smoke, resulting in the urgent evacuation of the Airbus A330-323 P&W turbofan engine in 2016 at London Heathrow Airport [10]. Besides the substantial benefits of seals on aero-engine performance, seal malfunctioning issues have highlighted how seals play an important role in aircraft. Thus, this study aims to shed light on the macro mechanical properties of fabric rubber composite seals of interest under different deformation modes, providing reliable numerical models to support composite seal design.

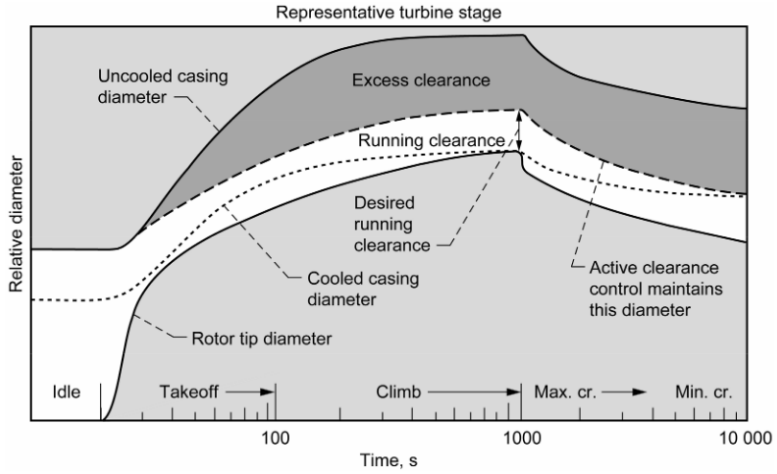

Figure 1: TCC effect on HPT blade tip clearance [7]

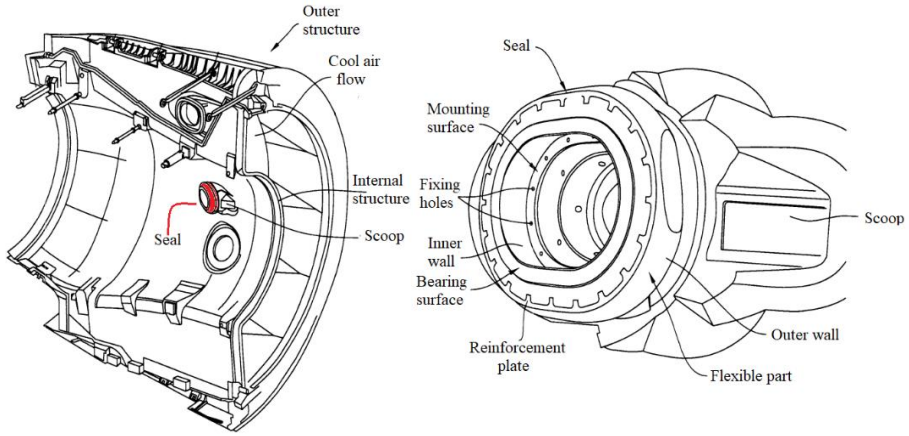

Figure 2: Turbine case cooling seal (left) and zoom on the seal (right) [11]

Fabric rubber composite seals usually include several layers of fabric reinforcement to provide stiffness, fireproofing, and abrasion resistance, as seen from a "P" seal drawing in Fig. 3. Thus, the composite exhibits anisotropic properties on top of hyperelastic, viscoelastic, and Mullins effects [12]. In this study, a set of coupon tests has been performed on pure rubber and plain-wave glass-fabric-rubber composites, accounting for different fabric orientations to characterize anisotropy. In particular, the campaign included uniaxial and equibiaxial tensile tests and uniaxial and planar compression tests for pure rubber and uniaxial tensile tests for composites. Then, the test results of pure rubber are used to identify invariant-based isotropic hyperelastic material models' parameters such as Neo-Hookean [13], Mooney [14]-Rivlin [15], and Ogden [16]. Furthermore, Spencer's theory [17] proposes some pseudo-invariants, based on the principal invariants defined with vectors, to account for anisotropy introduced by fabric reinforcement, analytically estimating the contribution of fabric layer in terms of strain energy. One of the most used anisotropic hyperelastic material models based on Spencer's theory is the Holzapfel-Gasser-Ogden (HGO) [18] model whose strain energy density function is given in Table 1 with other similar models. The material parameters of the anisotropic hyperelastic constitutive models are then identified from the coupon test results of fabric rubber composites. Finally, the anisotropic material models presented in Table 1 are scripted and implemented into Abaqus using UANISOHYPER_INV subroutine. It should be noted that the first parts of the strain energy potentials, i.e., defined by principal invariants, presented in Table 1 belong to isotropic hyperelasticity and the rest of the potential terms to account for fabric contributions.

Since most seals undergo bending deformation to provide sufficient sealing between the counterparts as seen in Fig. 2 from the TCC seal, pointing out that the bending behavior of fabric rubber composites is a crucial validation step in providing reliable numerical models for the composite seals. Hence, an in-

plane driven material identification methodology is developed to account for anisotropy and then implemented into Abaqus. Having preliminary results of bending tests reported, this study paves a path on the future bending behavior studies of fabric rubber composites with the developed methodology.

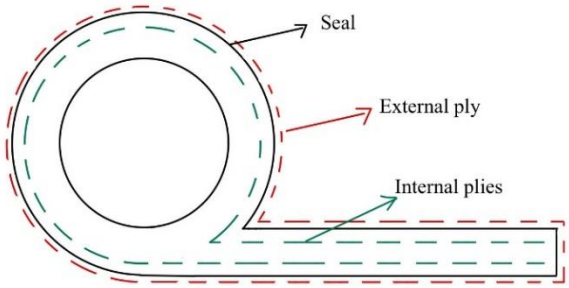

Figure 3: Conventional P-section seal cross-section view

Reference	Strain energy functions
HGO [18]	$W(I_1, I_4, I_6)$ $W = C_{10}(\bar{I}_1 - 3) + \frac{k_1}{2k_2}\sum_{i=4,6}\{\exp[k_2(\bar{I}_i - 1)^2] - 1\}$
Dong et al. [19]	$W(I_1, I_4, I_6)$ $W = C_{10}(\bar{I}_1 - 3) + C_{01}(\bar{I}_2 - 3) + \frac{k_1}{2k_2}\sum_{i=4,6}\left[e^{k_2(\bar{I}_i-1)^2} + \frac{k_2}{4}(\bar{I}_i - 1)^2 - 1\right]$
Gong et al. [20]	$W(I_1, I_4, I_6, I_8)$ $W = C_{10}(\bar{I}_1 - 3) + C_{01}(\bar{I}_2 - 3) + \frac{k_1}{2k_2}\sum_{i=4,6}\left[e^{k_2(\bar{I}_i-1)^2} + \frac{k_2}{4}(\bar{I}_i - 1)^2 - 1\right] + k_3(\bar{I}_8)^2$

Table 1: Constitutive models for fabric rubber composites

2 EXPERIMENTAL CAMPAIGNS

In this section, an experimental campaign is performed to characterize the mechanical behavior of pure rubber and fabric reinforced rubber composite under various loading conditions. In a first step, coupon tests enable to access materials response whereas in a second step, structural behavior is investigated through three points bending tests.

The vulcanized rubber and plain-wave glass fabric was processed at Elanova Laboratory in Paris. A set of moving-die-rheometer (MDR) tests was carried out for the vulcanized rubber subjected to different temperatures as per ISO3417, optimizing the manufacturing process parameters such as vulcanization temperature and duration. The test has revealed that the 100% vulcanization is secured after 20 min under 150°C. Accordingly, 2 mm silicone rubber sheets were vulcanized with a compression moulding setup under 150°C for 20 min while the 3 mm thick composites with one layer of composite sheets were kept 30 min under the same temperature. In addition, a 15 mm thick composite plate with 3 layers of 0.2 mm-thick glass fabric evenly placed through the thickness, keeping the fabric orientations identical for all layers, was also processed within the same setup for 45 min under 150°C. In addition, a different die was utilized to process pure rubber cylindrical specimens to be tested under compression. Lastly, the average density of pure rubber was measured as 1.289 g/cm3, while that of composite was found to be 1.333 g/cm3. Consequently, the processed materials were cut by die whose precision is regularly validated at Elanova laboratory.

2.1 Coupon tests

In order to check that the material model applies to any deformation modes, four different deformation modes in Table 2, i.e., uniaxial tensile (UT) and compression (UC), planar compression (CPL), and equibiaxial tensile (ET), were considered for pure rubber testing campaigns. VMQ represents silicone rubber while CVMQ represents composite silicone. The results of the above-mentioned tests on

pure rubber are plotted in Figure 4. As expected, the responses of the equibiaxial tensile and planar compression are stiffer than that of uniaxial tensile and uniaxial compression, respectively. A small dispersion of the uniaxial tensile test results would be caused by the unidirectional manual mixing procedure of unvulcanized rubber. Overall, the repeatability of the tests, with a small dispersion margin, shows the reliability of the tests.

Initial state	Dimensions and Material	Boundary conditions	Final state
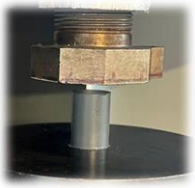	Diameter 18 mm Height 25 mm Pure rubber VMQ	Uniaxial compression (UC) 8 N pre-load 0.25 mm/min loading pace	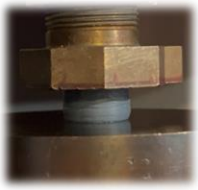
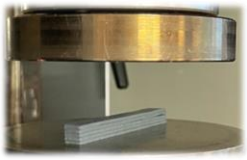	Size 10x10x100 mm Pure rubber VMQ	Planar compression (CPL) 8 N pre-load 0.10 mm/min loading pace	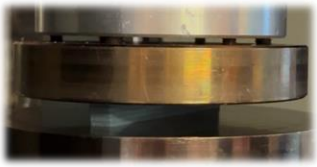
	Size 2x10x60 mm Pure rubber VMQ	Uniaxial tensile (UT) 0.6 N pre-load 0.6 mm/min loading pace	
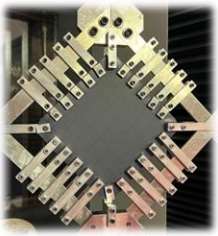	Size 2x110x110 mm Pure rubber VMQ	Equibiaxial tensile (ET) 2 N pre-load 1.10 mm/min	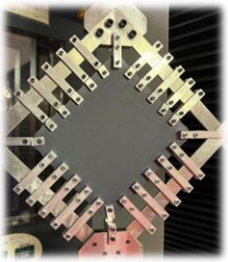
	Size 3x30x180 mm Composite 1 layer of glass fabric (CVMQ) 0 and 45 degree fabric orientations	Uniaxial tensile (UT) 8 N pre-load 1.8 mm/min	

Table 2: Coupon test matrix for pure rubber and composite

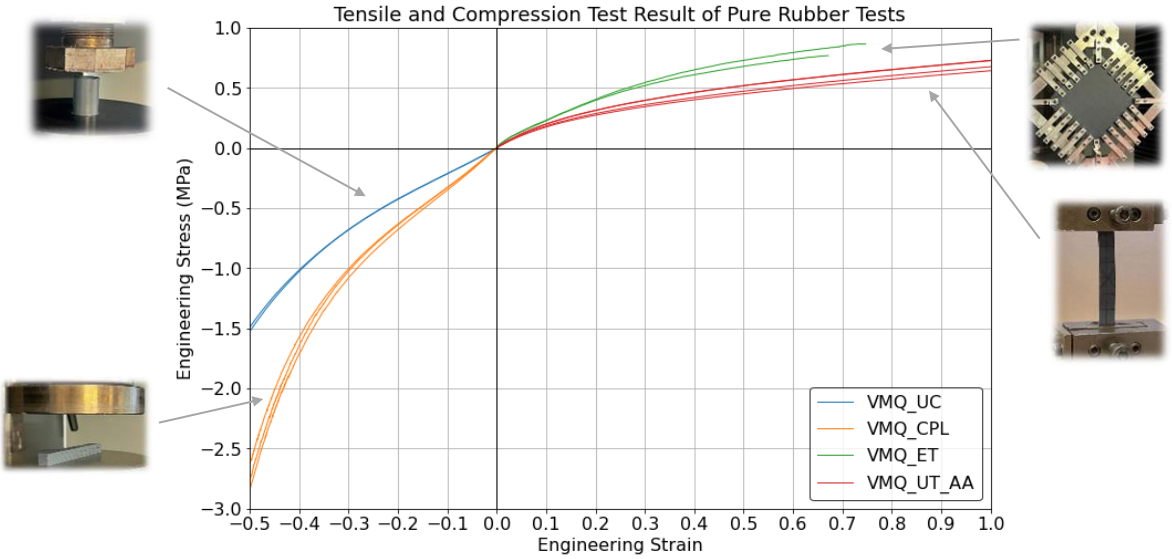

Figure 4: Tests results of pure rubber specimens under various loading conditions

On the other hand, the composite specimens were tested under 2 different fabric orientations, i.e., 0 and 45 degrees, to account for the anisotropy. The initial and final states of the tests as well as boundary conditions and dimensions were shared in Table 2. The test results of the composite with 2 different fabric orientations were plotted in Figure 5 where CVMQ_UT_0 indicates a 0-degree fabric-orientated composite while CVMQ_UT _45 is for 45-degree fabric-oriented composites. It can be clearly seen in Figure 5 that the material is highly anisotropic and non-linear, especially in the 45-degree case where the fabric is free to shear.

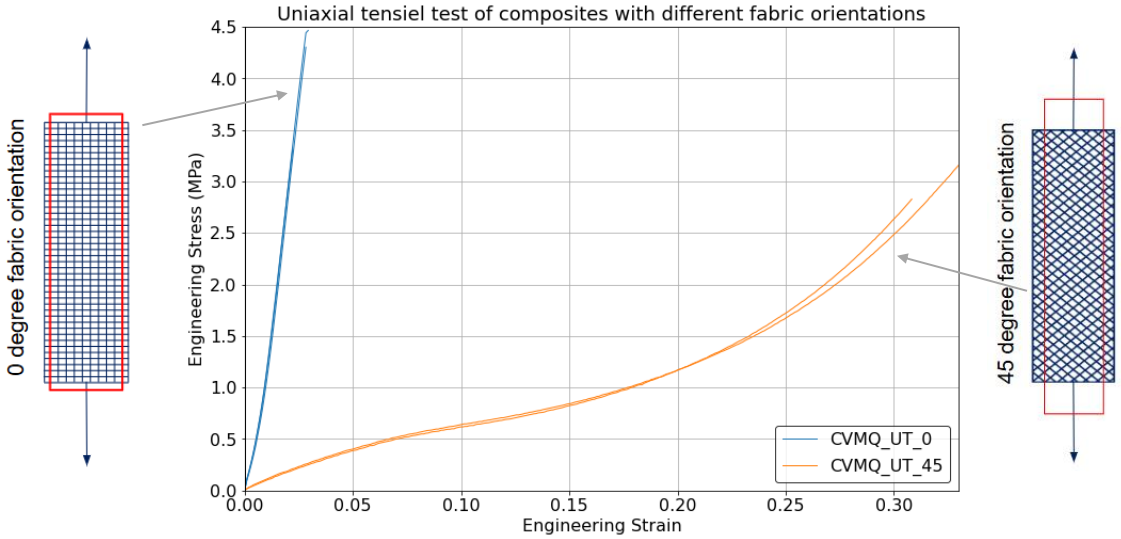

Figure 5: Tests results of composite specimens with one layer of glass fabric

Finally, a set of tests on pure rubber and composite with one layer of glass fabric has been conducted to initiate material modeling process that is going to be detailed in the following sections.

2.2 Three points bending campaign

Three-point bending tests have been carried out on composite specimens that include 3 layers of plain-wave glass fabric whose warp and weft directions are identical in all 3 layers. The experiments consider two different fabric orientations, i.e., 0- and 45-degree fabric orientations according to the axis along the length of specimens. The specimens with the dimensions of 15×15×70 mm were subjected to

0.5 mm/min displacement at the middle of the 50 mm middle span, as illustrated in Figure 6. The specimens were loaded till 6 mm middle displacement and the force output was recorded for each sample. The three point bending test results re plotted in Fig. 7. There is a clear difference between the results with the change of fabric orientation. The maximum load measure at 6 mm mid-span displacement is 37.22 N for the composite with 0-degree fabric orientation while it is 28.37 N for the composite with 45-degree orientation, indicating 30% increased force from 0 to 45 degree orientations.

.

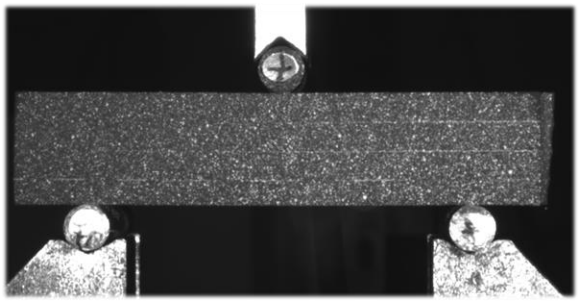

Figure 6: Initial state of 3-point bending test setup of a composite with 3 layers glass fabric

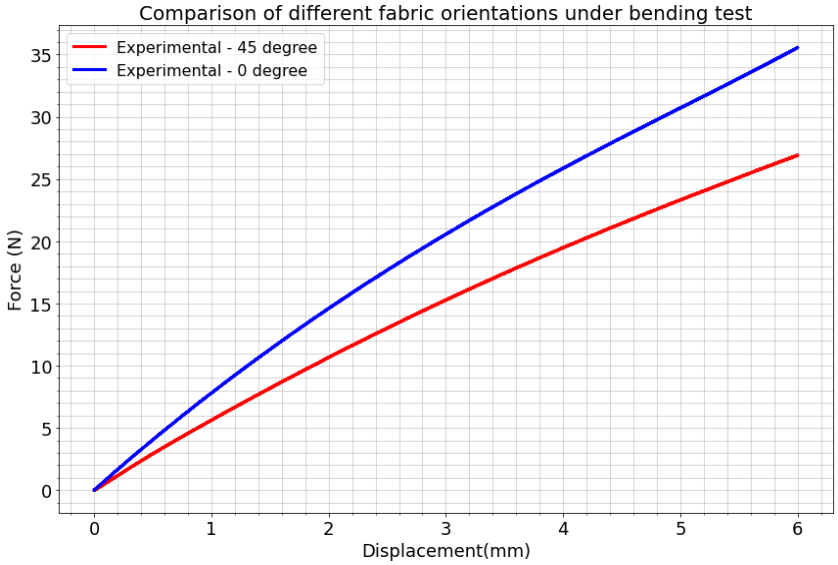

Figure 7: Three point bending test setup of composite specimens with 3 layers glass fabric

3 MODELING STRATEGY AND MATERIAL PARAMETER IDENTIFICATION

3.1 Constitutive model

Cauchy stress tensor can be defined in terms of strain energy as follows

$$\sigma = \frac{2}{J}\boldsymbol{F}\cdot\frac{\partial W}{\partial \boldsymbol{C}}\cdot\boldsymbol{F}^{T} - p\boldsymbol{I} \tag{1}$$

where W is strain energy function, $\boldsymbol{F} = \partial \boldsymbol{x}/\partial \boldsymbol{X}$ is deformation gradient, $\mathbf{C} = \boldsymbol{F}^{T}\cdot\boldsymbol{F}$ is right Cauchy-Green deformation tensor, $J = \det(\boldsymbol{C})$ is compressibility term, p is arbitrary pressure, and $\boldsymbol{I}$ is an identity tensor. The strain energy function W is defined as a function of the principal strain invariants for isotropic hyperelasticity and also as a function of pseudo-invariants to account for anisotropy as follows

$$W = W(I_1, I_2, I_3, I_4, I_6, I_8, I_i) \tag{2}$$

The first three invariants are the principal invariants and are defined as follows

$$I_1 = \mathrm{tr}\mathbf{C}$$
$$I_2 = \frac{1}{2}[(\mathrm{tr}\mathbf{C})^2 - \mathrm{tr}(\mathbf{C}^2)] \quad (3)$$
$$I_3 = \det(\mathbf{C})$$

I_4 and I_6 are the pseudo-invariants that account for fiber stretches in the two fiber directions. Moreover, I_8 is an interaction term that characterizes the interaction between rubber and fabric accounting shearing behavior between materials. The pseudo-invariants are derived from the vector definitions, N and M, aligned with the warp and weft directions of the fabric, on top of Cauchy-Green deformation tensor C. Having two vectors in the directions of two perpendicular fiber families, N and M vector expressions with respect to the Cartesian axes X and Y, are

$$\mathrm{N} = \begin{bmatrix} \sin\alpha \\ -\cos\alpha \\ 0 \end{bmatrix}, \mathrm{M} = \begin{bmatrix} \cos\alpha \\ \sin\alpha \\ 0 \end{bmatrix} \quad (4)$$

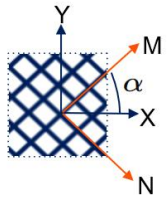

Figure 8: (N, M) vectors used to define the warp and weft directions of the fabric

Finally, based on the above-described vectors and the deformation tensor, the pseudo-invariants are derived with double-dot (:) and dyadic product ($\otimes$) as follows

$$I_4(\mathrm{M}) = \mathbf{C}:\mathrm{M}\otimes\mathrm{M},\quad I_6(\mathrm{N}) = \mathbf{C}:\mathrm{N}\otimes\mathrm{N},\quad I_8(\mathrm{M},\mathrm{N}) = \mathbf{C}:\mathrm{M}\otimes\mathrm{N} \quad (5)$$

Furthermore, considering the loading modes, e.g., uniaxial tensile and planar compression, one can easily define the deformation gradient for incompressible isotropic materials. In a specific case of uniaxial loading conditions and incompressible isotropic material, the deformation gradient is written as $F = \boldsymbol{diag}[\lambda, \lambda^{-\frac{1}{2}}, \lambda^{-\frac{1}{2}}]$. It should be noted that the second and third components of the deformation gradient become equal due to isotropy and incompressibility assumption. However, in the case of the anisotropic materials, obtaining deformation gradient is not a straight-forward step and requires an update of the deformation gradient at every load step. This paper will delve deeper into this topic in the following identification process.

In addition to the anisotropic strain energy functions provided in the introduction, the isotropic incompressible strain energy functions used in this study are listed in Table 3. It should be noted that the incompressibility assumption makes the third principal invariant zero ($I_3 = 0$).

Model Name	Strain energy potentials
Neo-Hookean [13]	$W = C_{10}(\bar{I}_1 - 3)$
Mooney [14]-*Rivlin* [15]	$W = C_{10}(\bar{I}_1 - 3) + C_{01}(\bar{I}_2 - 3)$
Ogden [16]	$W = \sum_{p=1}^{N} \frac{\mu_p}{\alpha_p}(\lambda_1^{\alpha_p} + \lambda_2^{\alpha_p} + \lambda_3^{\alpha_p} - 3)$

Table 3: Constitutive models for isotropic materials such as pure rubber

Consequently, the Cauchy stress tensors are derived substituting these potentials into Equation 1. Applying simple deformation modes, this method allows identification of the material parameters of the constitutive models for the material of interest.

3.2 Identification of material parameters

The identification process of the material parameters was achieved by minimizing, in the sense of least squares, the difference between the stress and strain curves between experimental results on uniaxial tensile loading mode and the analytical formulations of the models. Pure rubber models were identified prior to composites. For that purpose, a Python program, relying on the trust region optimization algorithm available in SciPy library [21] was developed. To have a complete stress equation, upon substituting all the components into Equation 1, one can calculate the arbitrary pressure p knowing that stress in the thickness direction is zero ($\sigma_{33}=0$) for all the loading conditions used in this study. Having p substituted back in Equation 1, the equation now is ready for the optimization process for isotropic hyperelastic models. On contrary, obtaining deformation gradient F is not straightforward for anisotropic hyperelasticity due to anisotropy. For example, considering incompressibility, the deformation gradient for the uniaxial loading case is now a function of first and second principal stretches due to possible inequality of second and third principal stretches because of anisotropy, seen below. Thus, at every step of imposed λ_{11}, λ_{22} was estimated by solving high order non-linear equation for $\sigma_{22}=0$. This equation is numerically solved at every λ_{11} step since there is no direct analytical solution for such complex equations.

$$\mathbf{F}_{\text{uniaxial}} = \begin{bmatrix} \lambda_{11} & 0 & 0 \\ 0 & \lambda_{22} & 0 \\ 0 & 0 & (\lambda_{11}\lambda_{22})^{-1} \end{bmatrix} \tag{6}$$

Based on the identification procedure explained above, one can obtain all stress equations for all above-mentioned material models with each given loading condition. As examples, only the stress equations of isotropic Mooney [14]-Rivlin [15] and anisotropic model by Gong et al. [20] under uniaxial boundary conditions are derived, in Equation 7 and 8, respectively. It is not possible here to state the stress equation for the Gong et al. [20] model explicitly for every updated deformation gradient. Thus, more general definitions are made in Equation 8.

$$\sigma_{11} = 2\left(C_{10} + \frac{C_{01}}{\lambda_{11}}\right)\left({\lambda_{11}}^2 - \frac{1}{\lambda_{11}}\right) \tag{7}$$

$$\boldsymbol{\sigma} = 2[W_1\mathbf{C} - W_2\mathbf{C}^{-1} + I_4W_4\mathbf{M}\otimes\mathbf{M} + I_6W_6\mathbf{N}\otimes\mathbf{N} + \frac{W_8(\mathbf{M}\otimes\mathbf{N}+\mathbf{N}\otimes\mathbf{M})}{2}] \tag{8}$$

where **M** and **N** are now tensors in which the above defined vectors multiplied with deformation gradient and its transpose as described in Equation 1 and W_i is the derivation of strain energy potential with respect to i^{th} strain invariant. Based on the identification performed on pure rubber, one can now identify the material constants associated with anisotropy (k_1, k_2, k_3 in Table 1). Remembering that I_4 and I_6 pseudo-invariants account for fiber extensions in fiber directions, associated k_1 and k_2 parameters can be then identified based on the uniaxial tensile test of the composite with 0-degree fabric orientation. The parameter k_3 associated with I_8 is optimized based on the uniaxial tensile test of the composite with 45-degree fabric orientation.

Furthermore, the above described and derived constitutive equations were scripted in Fortran and implemented into Abaqus using the UANISOHYPER_INV material subroutine. The developed material subroutines were then used to simulate composite tests with the same conditions, checking the subroutines. It must be noted that all the simulations employed implicit solution scheme and 0.5 mm hybrid brick elements considering geometric non-linearity assumption.

The material parameter identification process has resulted in material parameters presented in Table 4. Simulating the same coupon test conditions, the results were evaluated comparatively with experimental and analytical results. The numerical results with identified k_1 and k_2 parameters for the HGO [18] model are plotted in Fig. 9. Even if the numerical and analytical curves are in satisfactory agreement in this case of composite with 0 degree fabric orientation under tensile, it can be clearly seen that the model underestimates the material response for the 45-degree fabric orientation case. A very

similar observation was made for the model of Dong et al. [19] where no improvement in 45-degree case was observed, seen in Fig. 10 despite the new terms added into both isotropic and anisotropic parts of the strain energy function. Moreover, the parameter k_3 was identified to account for the shearing behavior between fabric and rubber. As seen in Fig. 11, the inclusion of I_8 resulted in improved results, which indicates the importance of modelling the shearing behavior of the composite with the additional pseudo-invariant. The identified material constants and the error metrics of the optimization studies were also shared in Table 4. In Table 5, one can easily notice the similar outcomes in the stress distribution results of the simulations at two different stretch values for Dong et al. [19] and Gong et al. [20] models with 45 degree fabric orientation, resulting in higher stress in Gong et al. [20] model around the transition zone as a result of the inclusion of shearing parameter.

Model Name	Strain energy functions
HGO [18]	$C_{10}(MPa) = 0.201\,,\quad k_1(MPa) = 28.72,\quad k_2 = 79.34,\quad ,\ R^2 = 0.639$
Dong et al. [19]	$C_{10}(MPa) = 0.166\,,\quad C_{01}(MPa) = 0.0352$ $k_1(MPa) = 23.02\,,\quad k_2 = 96.16,\quad R^2 = 0.705$
Gong et al. [20]	$C_{10}(MPa) = 0.166,\quad C_{01}(MPa) = 0.0352$ $k_1(MPa) = 23.02\,,\quad k_2 = 96.16,\quad k_3 = 0.279,\quad R^2 = 0.974$

Table 4: The identified material parameters for each material model

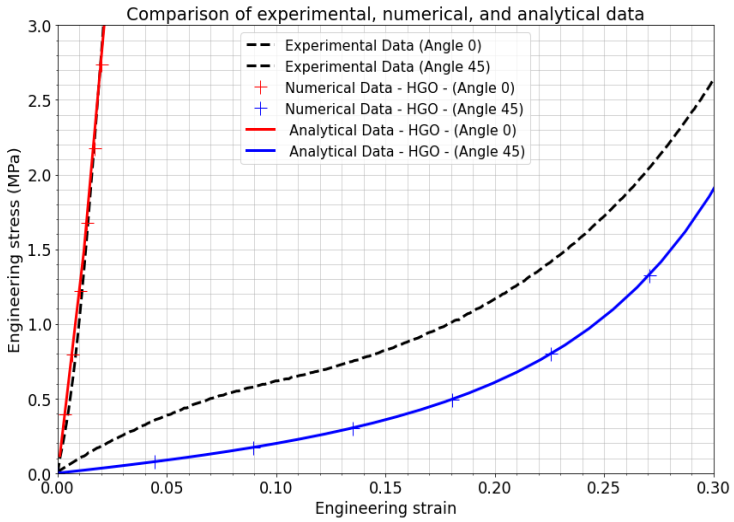

Figure 9: Analytical and simulation results of the HGO [18] model with experimental results

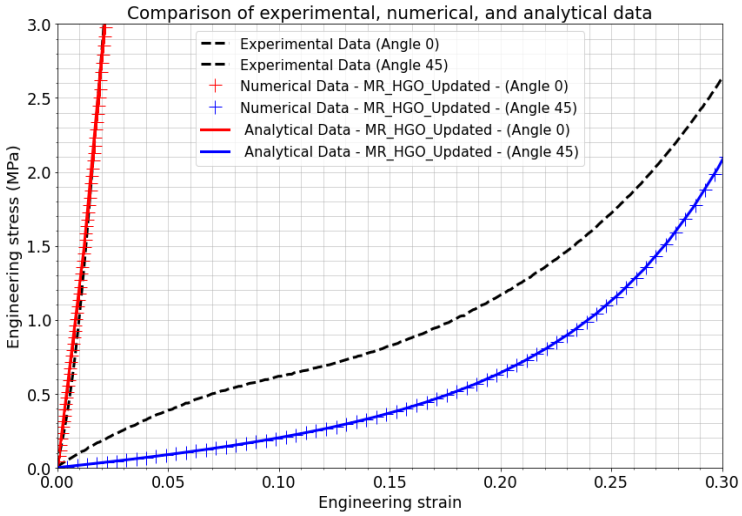

Figure 10: Analytical and simulation results of the *Dong et al.* [19] model with experimental results

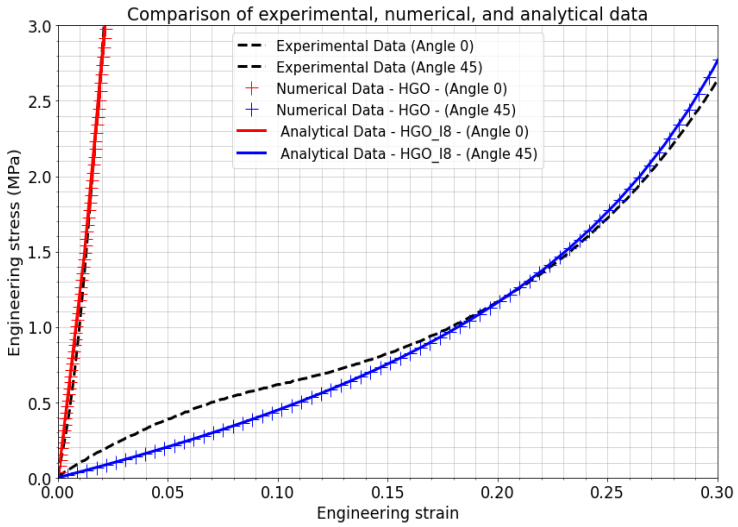

Figure 11: Analytical and simulation results of the *Gong et al.* [20] model with experimental results

S11(MPa)	Stress distributions

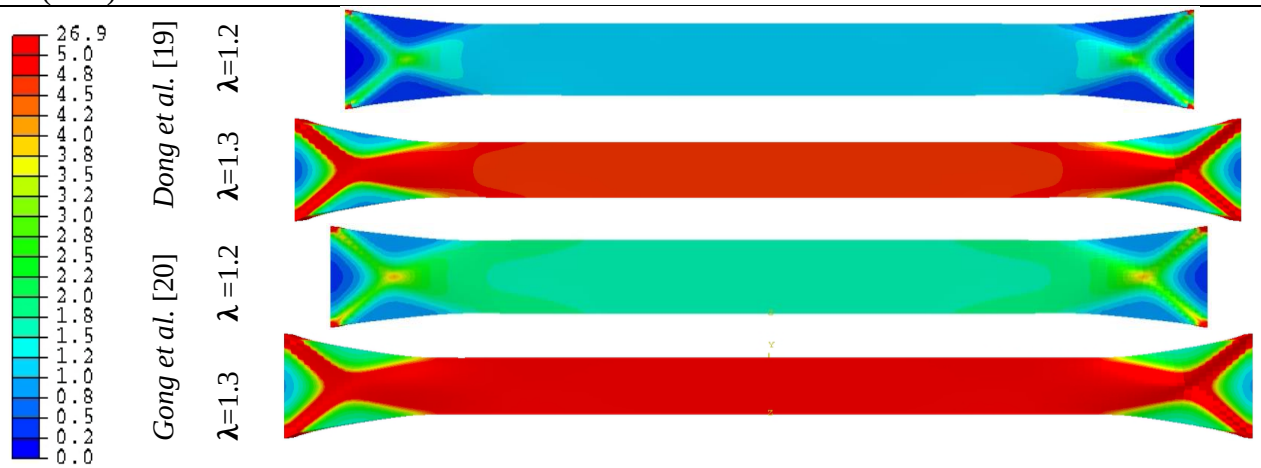

Table 5: Stress distribution of composites with 45-degree fabric-oriented under uniaxial tensile loading

4 CONCLUSIONS

In this paper several hyperelastic models, dedicated to pure rubber and fiber reinforced rubber, have been studied. In a first step, the model has been described, and the stress equations have been derived on specific loading cases of interest for identification purposes. Secondly, an identification process of pure rubber and composite materials has been conducted to obtain material parameters. Compared with the experimental results, the capabilities of different anisotropic material models, for composite modeling, were highlighted. The material models that do not include pseudo-invariant I_8 to account for shearing behavior between rubber and fabric are clearly seen incapable of reproducing material response especially for 45-degree fabric-oriented composite specimens. Moreover, the material model with I_8 defined resulted in satisfactory results in terms of the reproduction of material response. In the third step, the models with the identified material parameters were implemented in a finite element implicit framework using material subroutines. The composite simulations carried out with the developed subroutines under uniaxial loading conditions have resulted in a satisfactory mechanical response in comparison with experimental and analytical data. To conclude, this numerical modeling methodology provided and the 3-point bending tests pave the path for modeling bending behavior of fabric rubber composites for further studies.

REFERENCES

[1] P. H. Dunlap, « An Overview of Advanced Elastomeric Seal Development and Testing Capabilities at NASA Glenn Research Center », in *50th AIAA/ASME/SAE/ASEE Joint Propulsion Conference*, Cleveland, OH: American Institute of Aeronautics and Astronautics, juill. 2014. doi: 10.2514/6.2014-3599.

[2] Y. Fu et Y. Dong, « Evaluation of Key Performance of Aircraft Fabric Rubber Seal During Flight », *J. Aircr.*, vol. 58, nº 5, p. 1154-1167, sept. 2021, doi: 10.2514/1.C036331.

[3] M. F. Aksit, R. E. Chupp, O. S. Dinc, et M. Demiroglu, « Advanced Seals for Industrial Turbine Applications: Design Approach and Static Seal Development », *J. Propuls. Power*, vol. 18, nº 6, p. 1254-1259, nov. 2002, doi: 10.2514/2.6060.

[4] R. C. Bill, « Wear of Seal Materials Used in Aircraft Propulsion Systems », *Wear 59*, p. 165-189, 1980.

[5] H. Nishina, « Trends in Automotive Sealing Materials Technology », *Int. Polym. Sci. Technol.*, vol. 35, nº 3, p. 51-60, mars 2008, doi: 10.1177/0307174X0803500315.

[6] S. Lattime et B. Steinetz, « Turbine Engine Clearance Control Systems: Current Practices and Future Directions », in *38th AIAA/ASME/SAE/ASEE Joint Propulsion Conference & Exhibit*, Indianapolis, Indiana: American Institute of Aeronautics and Astronautics, juill. 2002. doi: 10.2514/6.2002-3790.

[7] R. E. Chupp, R. C. Hendricks, S. B. Lattime, et B. M. Steinetz, « Sealing in Turbomachinery », *J. Propuls. Power*, vol. 22, nº 2, p. 313-349, mars 2006, doi: 10.2514/1.17778.

[8] D. L. MORRILL, « TURBINE CASE COOLING SYSTEM », US 2016/0003151A1

[9] S. Shabbir, « Aerospace Sealing Technology for Maintenance, Repair and Overhaul of engines: a review », 2019.

[10] A. P. S. U. Govt., « Aircraft Incident Report 12/2017 N276AY EW/C2016/06/02 », 2017.

[11] B. Serge, « Joint d'étanchéité à appui intégré », FR2920218A1, 27 février 2009 [En ligne]. Disponible sur: https://patents.google.com/patent/FR2920218A1/fr

[12] L. Mullins, « Effect of Stretching on the Properties of Rubber », *Rubber Chemistry and Technology*, p. 281-300, 1948.

[13] L. R. G. Treloar, « The elasticity of a network of long-chain molecules—II », *Trans Faraday Soc*, vol. 39, nº 0, p. 241-246, 1943, doi: 10.1039/TF9433900241.

[14] M. Mooney, « A Theory of Large Elastic Deformation », *J. Appl. Phys.*, vol. 11, nº 9, p. 582-592, sept. 1940, doi: 10.1063/1.1712836.

[15] R. S. Rivlin, « Large elastic deformations of isotropic materials IV. further developments of the general theory », *Philos. Trans. R. Soc. Lond. Ser. Math. Phys. Sci.*, vol. 241, nº 835, p. 379-397, oct. 1948, doi: 10.1098/rsta.1948.0024.

[16] R. W. Ogden, « Large deformation isotropic elasticity – on the correlation of theory and experiment for incompressible rubberlike solids », *Proc. R. Soc. Lond. Math. Phys. Sci.*, vol. 326, nº 1567, p. 565-584, févr. 1972, doi: 10.1098/rspa.1972.0026.

[17] A. J. M. Spencer, *Continuum Theory of the Mechanics of Fibre-Reinforced Composites*. Vienna: Springer Wien, 2014.

[18] G. A. Holzapfel, T. C. Gasser, et R. W. Ogden, « A new Constitutive Framework for Arterial Wall Mechanics and a Comparative Study of Material Models », in *Cardiovascular Soft Tissue Mechanics*, S. C. Cowin et J. D. Humphrey, Éd., Dordrecht: Kluwer Academic Publishers, 2004, p. 1-48. Consulté le: 16 juillet 2024. [En ligne]. Disponible sur: http://link.springer.com/10.1007/0-306-48389-0_1

[19] Y. Dong, X. Yao, H. Yan, L. Yuan, et H. Yang, « Macro- and mesoscopic mechanical properties of complex fabric rubber composite under different temperatures », *Compos. Struct.*, vol. 230, p. 111510, déc. 2019, doi: 10.1016/j.compstruct.2019.111510.

[20] Y. Gong, X. Peng, Y. Yao, et Z. Guo, « An anisotropic hyperelastic constitutive model for thermoplastic woven composite prepregs », *Compos. Sci. Technol.*, vol. 128, p. 17-24, mai 2016, doi: 10.1016/j.compscitech.2016.03.005.

[21] P. Virtanen *et al.*, « SciPy 1.0: fundamental algorithms for scientific computing in Python », *Nat. Methods*, vol. 17, nº 3, p. 261-272, mars 2020, doi: 10.1038/s41592-019-0686-2.